Organic Electronics 51 (2017) 207–219

Contents lists available at ScienceDirect

Organic Electronics

journal homepage: www.elsevier.com/locate/orgel

Theoretical studying of basic photophysical processes in a thermally activated delayed fluorescence copper(I) complex: Determination of reverse intersystem crossing and radiative rate constants

LingLing Lv [a, *], Kun Yuan [a], YongCheng Wang [b]

[a] College of Chemical Engineering and Technology, Tianshui Normal University, TianShui, GanSu, 741001, China
[b] College of Chemistry and Chemical Engineering, Northwest Normal University, LanZhou, GanSu, 730070, China

ARTICLE INFO

Article history:
Received 3 August 2017
Received in revised form
10 September 2017
Accepted 10 September 2017
Available online 15 September 2017

Keywords:
Cu(dppb)(pz_2Bph_2)
Reverse intersystem crossing
Radiative rate constant
Thermal vibration correlation function (TVCF)

ABSTRACT

The photophysical properties of a mononuclear Cu(dppb)(pz_2Bph_2) complex have been investigated by employing the thermal vibration correlation function (TVCF) approach. The harmonic oscillator model with origin displacement, distortion, and Duschinsky rotation effects for the potential energy surfaces are considered. Absorption spectrum obtained by the scalar relativistic density functional theory combined with restricted open-shell configuration interaction including spin-orbit coupling effects is in excellent agreement with the experimental data. We found that the intersystem crossing (ISC) from the first excited singlet state (S_1) to the triplet state (T_1) is forbidden by direct spin-orbit coupling at the first-order perturbation, but becomes allowed through combined with vibronic coupling. The reverse intersystem crossing (RISC) proceeds at a rate of $K_{RISC} = 3.98 \times 10^8\ s^{-1}$ at room temperature 300 K, which is about 6 order of magnitude larger than the mean phosphorescence rate, $K_{P,\,av} = 7.3 \times 10^2\ s^{-1}$. At the same time, the ISC rate $K_{ISC} = 3.06 \times 10^9\ s^{-1}$ is again about 3 order of magnitude larger than the fluorescence rate $K_F = 6.47 \times 10^6\ s^{-1}$. This implies that the S_1 state can be populated from the T_1 state, TADF should be observed and TADF decay time is $\tau(300\ K) = 2.32\ \mu s$ by fitting calculation. But at 30 K, the situation will change. The RISC rate becomes very small, about $K_{RISC} = 1.19 \times 10^1\ s^{-1}$, while the ISC rate only decreases slightly from $K_{ISC} = 3.06 \times 10^9\ s^{-1}$ to $K_{ISC} = 1.93 \times 10^9\ s^{-1}$. As a consequence, the Cu(dppb)(pz_2Bph_2) complex is highly attractive candidates for applications of TADF.

1. Introduction

During the past decades, extensive investigation of Organic light emitting diodes(OLEDs) have been thoroughly carried out because of the goal of realizing thin, stable display devices with fast responses and wide viewing angles [1,2]. Unfortunately, some of these materials used suffer from low electroluminescence quantum yield due to spin statistics [3,4]. During exciton recombination, they have random spin orientation, and the singlet and triplet colliding pairs are equally probable. Thus, the excitons are created in a 1:3 ratio of singlet to triplet since the triplet state has three spin angular projections ($M_S = 0, \pm1$) and the singlet has only one ($M_S = 0$) microstate. Therefore, the internal quantum efficiency (IQE) of the radiative decay from triplet excitons is limited to 75%; IQE for fluorescent OLEDs is limited to 25%, the so called singlet-triplet bottleneck. To break through this bottleneck, recently, one has found that thermally activated delayed fluorescence (TADF) emitters can effectively convert the lowest triplet state (T_1) into the lowest singlet state (S_1) through reverse intersystem crossing (RISC) when the temperature rises, which largely improves the efficiency of exciton utilization and even makes it reach 100% in principle [5–7]. Therefore, the development of TADF materials has become a research hot spot for OLED [1–8].

A crucial character of TADF material is ensuring a small energy splitting between the S_1 and T_1 states, $\Delta E(S_1\text{-}T_1)$. In this regard, TADF molecules have often been designed following a strategy such that their highest occupied molecular orbital (HOMO) and lowest unoccupied molecular orbital (LUMO) are spatially separated to reduce their wave function overlap and lead to small exchange energy [9]. For this situation, One of the most rich TADF subfields, cheaper first-row transition metals such as copper can be used. Cu(I) complexes are well suited because their excited states often

* Corresponding author.
E-mail address: lvling100@163.com (L. Lv).

http://dx.doi.org/10.1016/j.orgel.2017.09.017
1566-1199/

exhibit low-lying metal to ligand charge transfer (MLCT) states of ^{3}MLCT and ^{1}MLCT character. In this situation, a distinct charge separation between excited and non-excited electron occurs, which leads to the singlet-triplet splitting, $\Delta E(S_1\text{-}T_1)$, also the quantum mechanical exchange interaction becomes small. As a consequence, ISC and RISC between the lowest triplet and the lowest singlet are reasonably fast, and therefore a TADF is possible.

Recently, Cu(I) complexes exhibiting thermally activated delayed fluorescence have received increasing attention in the theoretical and applicable fields [10–16]. However, a thorough understanding of the basic principles for the TADF photophysical processes is still scarce. We all know that it is crucial to understand the ISC mechanism of the interconversion processes of $T_1 \leftrightarrow S_1$ for the TADF photophysical processes. But, it is astounding that this process is not fully understood. Spin-orbit coupling (SOC) interaction can provides a major mechanism for a spin-forbidden ISC radiationless transition. But in most cases, SOC between ^{3}MLCT and ^{1}MLCT of donor-acceptor Cu(I) complexes is very small (tends to zero) and forbidden. It is therefore unlikely for the interconversion processes of $T_1 \rightarrow S_1$ via RISC directly, especially in view of the large rate $K_{RISC} \approx 10^7\ s^{-1}$ reported [17]. Alternatively Ogiwara et al. [18] proposed that RISC is driven by hyperfine coupling with an electron's spin and the magnetic nuclei of its molecule induce ISC. However, the hyperfine coupling constants are very small, usually in the range of 10^{-4} meV, and it therefore also appears highly unlikely for the large rates. This way, vibronic effects on TADF may have to be taken into account.

Lately, Some efforts have been made to reveal the mechanism of RISC through theoretical calculations including vibrational motion [19–21]. For example, Penfold et al. observed that the spin-orbit coupling between ^{1}CT and ^{3}CT is mediated by the lowest local exciton triplet (^{3}LE) of donor in 2,8-di(10H-phenothiazin-10-yl) dibenzo[*b*,*d*]thiphene-5,5-dioxide using quantum dynamics simulations [20]. Marian et al. reported the photophysical properties of a cationic three-coordinate Cu(I) complex with a monodenate N-heterocyclic carbene ligand and a bidentate phenanthroline ligand using the combined density functional theory and multireference configuration interaction method (DFT/MRCI) [21]. The results that RISC rate is particularly temperature-dependent, and the RISC rate becomes very small, about 8 s^{-1} at 77 K. While the direct spin-orbit coupling between S_1 and T_1 is negligible.

In this work, we chose a typical Cu(I) complex TADF emitter, Cu(dppb)(pz_2Bph_2), where dppb = 1,2-bis(diphenylphosphino) benzene and pz_2Bph_2 = diphenylbis(pyrazol-1-yl) borate (Fig. 1) as an model because it has a wealth of photophysical and spectroscopic data in experiments [22,23]. The interconversion and decay rate constants of S_1 and T_1 have been quantitatively calculated by employing the thermal vibration correlation function (TVCF) rate theory in combination with the DFT/TD-DFT methods [24]. Absorption spectrum obtained by the scalar relativistic DFT combined with restricted open-shell configuration interaction(ROCIS) including spin-orbit coupling effects is in excellent agreement with the experimental data. The motivation would provide design routes for high-performing Cu(I) complex TADF materials by on deeper understanding of the $S_1 \leftrightarrow T_1$ ISC process.

2. Computation details and theoretical background

2.1. Geometry optimizations

The mononuclear Cu(dppb)(pz_2Bph_2) TADF molecule considered here are mostly donor-acceptor charge-transfer molecule, the range-separated corrected functionals CAM-B3LYP [25,26] along with Grimme's 2010 atom-pairwise dispersion correction [27] to density functional theory (DFT) with Becke-Johnson damping (GD3BJ) may compute better since B3LYP would significantly overestimate electron delocalization in the excited states. Therefore, optimization of the ground state and excited state structures were calculated using the CAM-B3LYP functionals as well as corresponding to time-dependent TD-CAM-B3LYP with 6-311+G(d,p) Gaussian-type basis set using Gaussian 09 package [28], followed by calculations of harmonic vibrational frequencies and normal modes to obtain equilibrium geometries and calculate thermal vibration correlation functions.

2.2. Excited state properties

On the basis of the CAM-B3LYP optimized structures, electronic vertical absorption were calculated with the parallel version of the combined DFT (CAM-B3LYP, or ωB97X-D3) and restricted open-shell configuration interaction with single excitations (DFT/ROCIS) method [29] by version 4.0 of the ORCA package [30]. This method includes the dynamic correlation from DFT as well as the static correlation from the ROCIS approach. The excitation energies and transition dipole moments for the absorption spectrum including SOC were obtained with SOC-quasi-degenerate perturbation theory (QDPT) [29]. Calculations with hybrid functionals used the RIJCOSX algorithm to speed the calculation of Hartree-Fock exchange [31]. For transition metal complexes, relativistic effects should be expected, which may have significant effect on the calculated spectra. Calculations of relativistic effects included the second-order Douglas-Kroll-Hess (DKH) correction and also taken into account picture change effects [32]. The scalar relativistically recontracted DKH-def2-TZVP(-f) basis set and the decontracted auxiliary def2/J Coulomb fitting basis sets with ORCA Grid5 was used for all atoms.

2.3. Spin-orbit coupling and zero-field splitting

The spin-spin dipole and SOC interactions for the open shell triplet geometry are considered with a Hamiltonian operating on zero-order triplet wave functions, which introduces some angular momentum into the ground state resulting in the zero-field splitting (ZFS) spin parameters axial *D* and rhombic *E*. SOC calculations

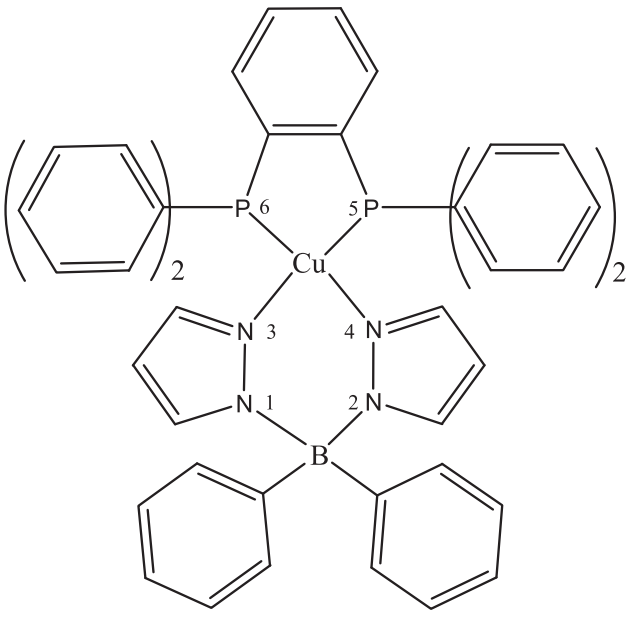

Fig. 1. Chemical structure of mononuclear Cu(dppb)(pz_2Bph_2) complex.

were performed on top of the above-mentioned DFT/ROCIS calculations combined with the framework of QDPT [29]. Herein, we employed an accurate multicenter spin-orbit mean-field(SOMF) of the Breit-Pauli SOC operator on all centers [33,34]. This operator explicitly takes care of the one- and two-electron parts and includes the spin-same-orbit as well as spin-other-orbit terms in its two-electron part. These calculations were performed with a key word of SOCFlags 1, 3, 3, 1 in the ORCA 4.0 program [30]. For comparison, SOC and the ZFS parameters are also calculated at the level of complete active space self consistent field (CASSCF) wave function.

2.4. Fluorescence and phosphorescence rates

For Fluorescence and phosphorescence rates or lifetimes, respectively, the DFT/ROCIS wave functions were calculated. Singlet-triplet transitions are strictly forbidden in the regime of an unrelativistic treatment, however, SOC interactions couple these states, resulting in nonzero probability of spin-forbidden transitions. The intensity of the spin-forbidden transition is proportion to the square of the $\mu(S_0 \leftarrow T_{1,\varsigma})$ transition moment. $\mu(S_0 \leftarrow T_{1,\varsigma})$ can be written as follow [35]:

$$\begin{aligned}\mu(S_0 \leftarrow T_{1,\varsigma}) &= \langle S_0|\mu_\alpha|T_{1,\varsigma}\rangle \\ &= \sum_n \frac{\langle S_0|\mu_\alpha|S_n\rangle\langle S_n|\widehat{H}_{SOC}|T_{1,\varsigma}\rangle}{E(T_{1,\varsigma}) - E(S_n)} \\ &\quad + \sum_m \frac{\langle T_{1,\varsigma}|\mu_\alpha|T_m\rangle\langle T_m|\widehat{H}_{SOC}|S_0\rangle}{E(T_m) - E(S_0)} \end{aligned} \quad (1)$$

where $T_{1,\varsigma}$ represents the ζ (= I, II, and III) spin sublevel of triplet T_1 state being subject to the ZFS induced by internal magnetic perturbations; μ_α is an electric dipole moment operator projection on the α axis; and $\widehat{H}_{SOC}$ is the SOC operator.

The electric transition dipole moments of the received spin-mixed wave functions can be used to calculate the rates according to eq. (2).

$$K_{r,\varsigma} = \frac{4e^2}{3c^3\hbar^4} \Delta E^3_{S_0 \leftarrow T_{1,\varsigma}} |\mu(S_0 \leftarrow T_{1,\varsigma})|^2 \quad (2)$$

wherein $\Delta E_{S_0 \leftarrow T_{1,\varsigma}}$ denotes a vertical emission energy.

Considering the vibronic coupling from origin displacements, distortions, and Duschinsky rotation within a multimode harmonic oscillator model, we adapt the thermal vibration correlation function (TVCF) method [24]. The spontaneous radiative decay rate with time-dependent form, K_r, is the integration of eq. (4):

$$\sigma(\omega, T) = \frac{4e^2}{3c^3\hbar^4} |\mu(S_0 \leftarrow T_{1,\varsigma})| \int e^{-i\omega t} e^{i\omega_{S_0 \leftarrow T_1} t} Z_i^{-1} \rho_{em}(t, T) dt \quad (3)$$

$$K_r = \int_0^\infty \sigma_{em}(\omega) d\omega \quad (4)$$

in which $Z_{T_1}^{-1} = \sum_{v=\{0_1,0_2,\ldots,0_N\}}^{\infty} e^{-\beta E_v^{T_1}}$ is the partition function, and N is the number of normal modes; the TVCF form is $\rho_{em}(t, T) = \mathrm{Tr}[e^{i\tau_{T_1}} \widehat{H}_{T_1} e^{i\tau_{S_0}} \widehat{H}_{S_0}]$ and can be solved analytically by multidimensional Gaussian integrations. Here, $\tau_i = -i\beta - (t/\hbar)$, $\tau_f = t/\hbar$, $\beta = (k_B T)^{-1}$, and $\widehat{H}_{T_1}(\widehat{H}_{S_0})$ is the harmonic oscillator Hamiltonian of the triplet (singlet) electronic state. These calculations were performed using the MOMAP program [36,37] combined with the ORCA 4.0 program [30].

2.5. Intersystem crossing rate constant

Similarly, the vibrational contributions to the ISC and RISC rates were also calculated using the MOMAP program [36,37]. Based on the time-dependent second-order perturbation theory and Born-Oppenheimer adiabatic approximation, thermal average ISC from initial T_1 electronic state with the vibrational quantum numbers v to the final S_1 electronic state with the vibrational quantum numbers u may be expressed as

$$K_{ISC} = \frac{2\pi}{\hbar} \left|\langle T_1|\widehat{H}_{SOC}|S_1\rangle\right|^2 Z_{T_1}^{-1} \sum_{v,u} e^{-\beta E_v^{T_1}} |\langle \Theta_{T_1,v}|\Theta_{S_1,u}\rangle|^2 \delta(E_{T_1,v} - E_{S_1,u}) \quad (5)$$

Here, $Z_{T_1}^{-1} = \sum_{v=\{0_1,0_2,\ldots,0_N\}}^{\infty} e^{-\beta E_v^{T_1}}$, N is the number of normal modes; the delta function δ is to keep the conservation of energy. Applying the Fourier transform of the δ function, eq. (5) is recast as

$$K_{ISC} = \frac{1}{\hbar^2} \left|\langle T_1|\widehat{H}_{SOC}|S_1\rangle\right|^2 \int_{-\infty}^{\infty} dt \left[e^{i\omega_{T_1,S_1} t} Z_{T_1}^{-1} \rho_{ISC}(t, T)\right] \quad (6)$$

where the TVCF form is $\rho_{ISC}(t, T) = \mathrm{Tr}[e^{i\tau_{S_1}} \widehat{H}_{S_1} e^{i\tau_{T_1}} \widehat{H}_{T_1}]$. The detailed derivation of these formulas is found in ref.22. The ISC and RISC rates were calculated for two temperatures, 30 K and 300 K. The time correlation function was integrated over a time interval of 0.01fs and a grid of 30000 points was chosen.

3. Results and discussion

3.1. The molecular geometries

The geometric structures of mononuclear Cu(dppb)(pz_2Bph_2) complex are shown in Fig. 2, and the Cartesian coordinate parameters of geometry are listed in Table S1 in the Supporting Information. The coordination geometry is distorted from the D_{2d} tetrahedral geometry that might be expected for a d^{10} metal ion. The dihedral angles between the two planes defined by the P5—Cu—P6 atoms and N1—Cu—N2 atoms are 87.60° for the ground state S_0. The parameters of the ground state equilibrium geometry are in good agreement with the experiment [23]. In the crystal structure, the Cu—N bond lengths are 2.011—2.018 Å, Cu—P bond is the length of 2.257 Å, while the calculated bond lengths of the Cu—N bond and Cu—P bond are 2.015 Å and 2.268 Å, respectively. The dihedral angles between the two planes defined by ∠N1-N2-P5-P6 are 87.48° in the experiment compared to a computed value of 87.60° [23]. Thus the structure of Cu(dppb)(pz_2Bph_2) is well reproduced at the CAM-B3LYP/6-311+G(d, p) level.

Structural changes upon the S_1 and T_1 states, predicted at the TD-CAM-B3LYP level, show that excitation includes mostly charge transfer involving the 3d metal orbitals (HOMO) and dppb ligand-centered π^*-orbital (LUMO). The Cu—P bonds are both elongated by about 0.09 Å in the S_1 and T_1 states compared with the structure of the S_0 state. The distortion changes of between the P5—Cu—P6 plane and N1—Cu—N2 plane are the strongest with the deviations being 28.05° and 29.09° in T_1 and S_1, respectively. However, the S_1 and T_1 geometries are very similar, with the largest deviation for the bond length being 0.01 Å and that for the bond angle being 0.1°. The intuitive pictures comparing the S_0, S_1 and T_1 geometries are shown in the second column of Fig. 2.

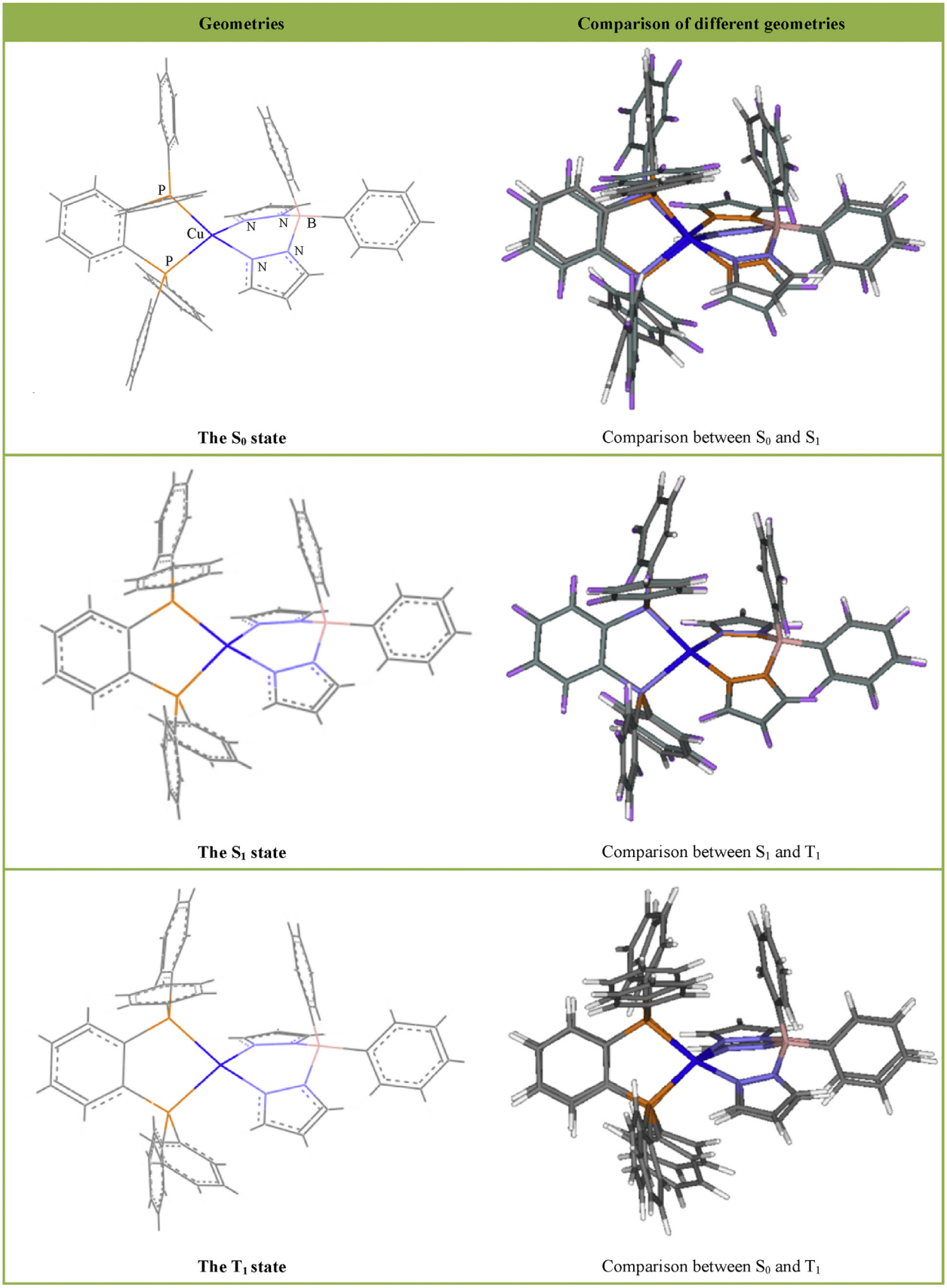

Fig. 2. Front view of the CAM-B3LYP optimized ground state geometry and TD-CAM-B3LYP optimized excited state geometries using the 6-311+G(d, p) basis set. The second column geometries are intuitive pictures comparing the S_0, S_1 and T_1 geometries for the mononuclear Cu(dppb)(pz_2Bph_2) complex.

3.2. Spin-free and spin-orbit theoretical absorption spectrum

The vertical spin-free absorption spectrum of the mononuclear Cu(dppb)(pz_2Bph_2) complex have been computed for the optimized S_0 geometry, schematically depicted in Table 1. The experimental absorption spectrum has been recorded in CH_2Cl_2 [22,23]. Very weak band 440 nm (≈2.81eV) was assigned to CT transition involving the 3d metal orbitals and dppb ligand-centered π*-orbital. The TDDFT and experimental spectra are seen to match perfectly from Table 1. The S_1 state lie 2.62 eV, and the excitation might gain some intensity through vibronic transition. The S_1 main configuration is single excitation from HOMO to LUMO (64.9%) and LUMO+1 (30.4%), for a molecular orbital scheme with graphical representations of the Kohn-Sham orbital densities, see Fig. 3. The HOMO has d/σ character originating from a linear combination of d_{xy}-like orbital of the copper atom with p orbitals of coordinating phosphorous atoms, whereas the LUMO and LUMO+1 are mainly distributed over the phenylene ring of the dppb ligand. It reveals a special excited state formation, that is MLCT process with the charge transfer from metal to an empty antibonding π* orbital of the dppb ligand. In the calculated spectrum, one can find the excitation with the strongest oscillator strength (f = 0.20683) at 3.12 eV. This $S_0 \rightarrow S_3$ excitation is dominated by a d/σ → σ*(diphenylphosphino) configuration. The remain three singlet excited states S_2, S_4, and S_5, are assigned to be of the obvious CT transition feature due to the spatial separation of the involved molecular orbitals, which leads to the relatively small oscillator strength f of the transition between S_0 and S_2, S_4, and S_5. Indeed, this is supported by the TD-DFT calculations giving f values (see Table 1).

Absorption spectra obtained at the scalar relativistic CAM-B3LYP(and ωB97X-D3)/ROCIS level and including SOC effects by means of QDPT is plotted in Fig. 4. It can be seen that the trend of the spectrum does not change significantly when SOC effects are included. Vital differences can be seen in line spectrum where any excitations gain oscillator strength due to singlet-triplet interaction. In principle, SOC may lead to the $S_0 \rightarrow T_m$ excitation in two different ways (see eq. (1)): the S_0 state can couple with triplet excited states, T_m. In this way, spin- and electric-dipole allowed excitations in the triplet manifold, from T_1 to T_m that mix with S_0 may contribute. Alternatively, the T_1 state couples with the excited singlet states, S_n, mixing in contributions from electric-dipole allowed excitations in the singlet manifold. Thus, the formally spin forbidden $S_0 \rightarrow T_m$ excitation is activated via SOC interaction. For the CAM-B3LYP method, at 498 nm (20049 cm^{-1}), and 489 nm (20413 cm^{-1}) at the ωB97X-D3 level, there is an excitation with substantial oscillator strength that has no correspondence in the spin-free spectrum. It is a $S_0 \rightarrow T_1$ excitation with some singlet excited state admixture. At the same time, SOC can involve magnetic interactions which splits the T_m manifold into three substates ($T_{m,\,(I,\,II,\,III)}$), i.e. ZFS, that are separated in energy in the absence of an applied field, see Fig. 4c and d.

3.3. Singlet-triplet splitting ΔE(S_1-T_1)

Through the above discussion, the S_1 and T_1 states have the same configurations, ^{1}MLCT and ^{3}MLCT, from d/σ → π* MLCT excitations. For TADF molecules, a key requirement is very small singlet-triplet splitting energy $\Delta E(S_1\text{-}T_1)$ between the S_1 and T_1 excited states. To choose an optimal calculation approach to evaluate $\Delta E(S_1\text{-}T_1)$, TD-DFT methods including B3LYP, M062X, and long-range correction functions (CAM-B3LYP, ωB97X-D3, LC-BLYP) at def2-TZVP(-f) basis set level were tested. These values are listed in Table S2. Compared to the experimental value of $\Delta E(S_1\text{-}T_1)$ = 370 cm^{-1} [22], it is clear that the CAM-B3LYP (371.0 cm^{-1}), B3LYP (379.1 cm^{-1}), and ωB97X-D3 (372.5 cm^{-1}) functions give the best prediction of $\Delta E(S_1\text{-}T_1)$ at the S_1 geometry.

It is well known that the S_1 and T_1 states with the same orbital configuration are separated by the exchange energy (J, also called as exchange coupling constant) as illustrated in eqs. (7) and (8) with ϕ_L and ϕ_H corresponding to the electron and hole orbitals involved in the transition, respectively [9]. Often ϕ_L is the LUMO and ϕ_H is the HOMO. Where the J values are relative with the spatial separation (r_1-r_2) and overlap integral of ϕ_L and ϕ_H at the S_0 state, higher overlap of HOMO and LUMO and smaller spatial separation lead to higher J and $\Delta E(S_1\text{-}T_1)$.

$$\Delta E(S_1\text{-}T_1) = E(S_1) - E(T_1) = 2J \tag{7}$$

$$J = \iint \phi_H^*(r_1)\phi_L(r_2)(1/r_1 - r_2)\phi_L^*(r_1)\phi_H(r_2)d_{r_1}d_{r_2} \tag{8}$$

Thus, in order to give a quantitative investigation, hole-electron overlap extent ($S_{h\text{-}e}$) and mean separation distance ($D_{h\text{-}e}$) of HOMO and LUMO associated of the S_1 and T_1 transitions can be calculated using the Multiwfn program [38], and calculated results are depicted in Fig. 5.

Along with photo excitation, intramolecular charge transfer of electron from ground state to excited state takes place for Cu(dppb)(pz_2Bph_2), in which sufficient spatial charge separation within the TADF is desired to enhance the subsequent charge transfer processes. It is evident that both S_1 and T_1 present a marked charge transfer by excitation, where significant electron density difference are observed between the Cu group (electron donor, the density deletion zone) and the dppb ligand (electron acceptor, the density increment region). The S_1 reveals a charge transfer (Q_{CT}) of 0.97 $e-$, which is slightly larger than 0.82 $e-$ by T_1; And charge transfer distances (D_{CT}) are 1.32 Å for S_1 and 1.07 Å for T_1 (see Fig. 5). These critical parameters revealed that both the S_1 and T_1 excitations have the net CT character.

The hole-electron overlap ($S_{h\text{-}e}$) and separation distance ($D_{h\text{-}e}$)

Table 1
Singlet-singlet transition electric dipole moments (in a.u.), transition energies (in eV), and their oscillator strength (f) of the mononuclear Cu(dppb)(pz_2Bph_2) complex at the TD-wB97X-D3/def2-TZVP(-f) level for the optimized S_0 geometry.

Excited State(n)	$\langle S_0\|\mu_x\|S_n\rangle$	$\langle S_0\|\mu_y\|S_n\rangle$	$\langle S_0\|\mu_z\|S_n\rangle$	$\Delta E_{S0\rightarrow Sn}$	f	TD-DFT weights
S_1	−0.137	−0.559	0.145	2.615	0.02256	HOMO→LUMO 64.9% HOMO→LUMO+1 30.4%
S_2	−0.685	−0.576	0.185	2.770	0.05676	HOMO→LUMO+1 65.9% HOMO→LUMO 32.6%
S_3	0.775	1.160	−0.872	3.118	0.20683	HOMO→LUMO+2 81.8% HOMO→LUMO+3 13.1%
S_4	−0.006	−0.434	−0.971	3.229	0.08965	HOMO→LUMO+3 84.3% HOMO→LUMO+2 13.9%
S_5	−0.300	0.327	−0.090	3.388	0.01702	HOMO-2→LUMO 36.5% HOMO→LUMO+4 48.0%

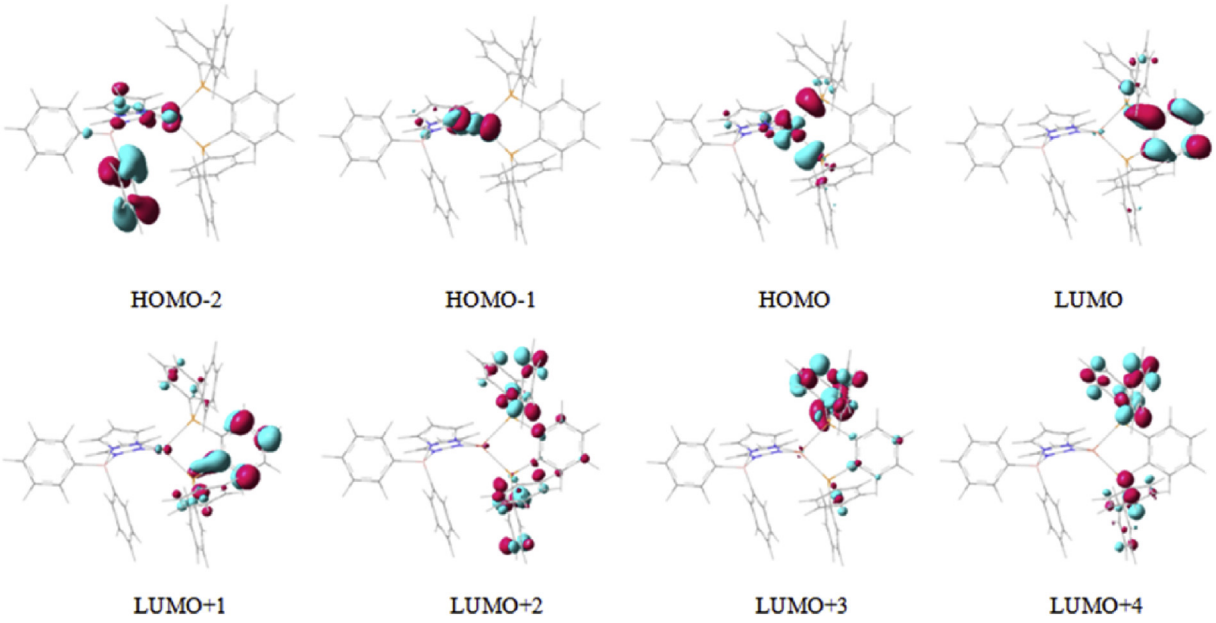

Fig. 3. Singlet-singlet transition orbitals of the mononuclear Cu(dppb)(pz_2Bph_2) complex.

were quantified successfully. As illustrated in Fig. 5, it was found that the S_1 and T_1 possess separated hole-electron with small $S_{h\text{-}e}$ and long $D_{h\text{-}e}$, leading to small $\Delta E(S_1\text{-}T_1)$. This is highly desirable in the TADF design as it leads to sufficient charge separation upon photoexcitation that in turn, reduces geminate recombination and facilitates TADF regeneration.

3.4. Phosphorescence and fluorescence

Fundamentally, $T_1 \rightarrow S_0$ phosphorescence emission is caused through perturbation of the pure spin states by SOC, which considers the intensity borrowing from spin-allowed electronic transitions, i.e., from $T_m \leftrightarrow T_1$ or $S_n \leftrightarrow S_0$. SOC is a relativistic property, and it can cause ZFS substates of the T_1 state have quite different radiative and nonradiative properties. However, detailed studies are only rarely found. Yersin et al. [22] have experimentally determined to ZFS values of less than 1 cm^{-1}. Our CAM-B3LYP/ROCIS calculation shows that $\Delta_{I,\ II} = 0.00\ cm^{-1}$ and $\Delta_{II,\ III} = 0.03\ cm^{-1}$, in good agreement with experiment, particularly using CASSCF methods the computed values of $D = 0.415\ cm^{-1}$ and $E = 0.064\ cm^{-1}$ ($\Delta_{I,\ II} = E$; $\Delta_{II,\ III} = D$) at the T_1 geometry, see Tables 2 and 3. ZFS is very small, the first T_I and second T_{II} triplet components are virtually degenerate, and the splitting between the T_{II} and T_{III} components amounts to less than 1 cm^{-1}. A correspondingly small value is only possible if SOC-induced mixing of higher-lying singlet or triplet MLCT states with the lowest triplet substates (T_I, T_{II}, and T_{III}) is very weak.

Phosphorescence and fluorescence rates or lifetimes, by only considering electronic transition through Einstein spontaneous emission formula without any involvement of vibronic couplings, respectively, have been calculated for both the S_1 and T_1 geometries, which is listed at Table 3. The calculated rates at the S_1 and T_1 geometries are quite similar. At the T_1 geometry, we find that the phosphorescence radiative rates of the three substates are $K_{P,\ I} = 8.26 \times 10^1\ s^{-1}$ ($\tau_I = 12.1$ ms), $K_{P,\ II} = 5.88 \times 10^2\ s^{-1}$ ($\tau_{II} = 1.7$ ms), and $K_{P,\ III} = 2.03 \times 10^3\ s^{-1}$ ($\tau_{III} = 493$ μs)), in reasonable agreement with experimentally measured values (which are τ_I, and $\tau_{II} = 7.7$ ms, $\tau_{III} = 470$ μs)) [22]. At a low temperature, these states are not thermally equilibrated because of very slow spin-lattice relaxation processes. With the increase of temperature, however, the spin-lattice relaxation processes become significantly faster and a fast thermalization of the three substates results, an averaged emission decay time τ_{av} can be calculated by the three individual decay times according to $\tau_{av} = 3(\tau_I^{-1} + \tau_{II}^{-1} + \tau_{III}^{-1})^{-1}$. From Table 3, the calculated mean for the three phosphorescence rate is $K_{P,\ av} = 9.01 \times 10^2\ s^{-1}$ ($\tau_{av} = 1109$ μs)) at the T_1 geometry, and the rate for the fluorescence is $K_F = 8.06 \times 10^6$ ($\tau_F = 124$ ns)), which are in good agreement with experimentally measured values of $\tau_{av} = 1200$ μs and $\tau_F = 180$ ns. For the S_1 geometry, we obtain values of $K_{P,\ av} = 1.15 \times 10^3\ s^{-1}$ ($\tau_{av} = 870$ μs)) and $K_F = 5.01 \times 10^6$ ($\tau_F = 199$ ns)).

3.5. RISC and TADF

Due to the small difference $\Delta E(S_1\text{-}T_1)$ between the S_1 and T_1 minima, TADF should, theoretically, be possible. In order to ascertainably take place, the S_1 state has to be repopulated. That means that the RISC rate has to be larger than the rates of radiative and nonradiative decay of the T_1 state to the S_0 state.

In the Franck-Condon approximation, ISC or RISC rate is directly proportion to the squared $T_1 \leftrightarrow S_1$ SOC element calculated for the relaxed geometry of the T_1 state. One can see that the S_1 and T_1 states have the same configurations and almost the equivalent weights, which lead to the spin forbidden intersystem crossing. It is well known that the SOC matrix element can be written as in terms of ladder operators [39] (eq. (9)).

$$\left\langle \phi_\mu \theta_\mu | L \cdot S | \phi_\nu \theta_\nu \right\rangle = \left\langle \phi_\mu | L_z | \phi_\nu \right\rangle \left\langle \theta_\mu | S_z | \theta_\nu \right\rangle + 0.5 \left\langle \phi_\mu | L_+ | \phi_\nu \right\rangle \left\langle \theta_\mu | S_- | \theta_\nu \right\rangle + 0.5 \left\langle \phi_\mu | L_- | \phi_\nu \right\rangle \left\langle \theta_\mu | S_+ | \theta_\nu \right\rangle \tag{9}$$

where L is the orbital angular momentum operator, and S is the spin operator; the ϕ is the space part of the molecular orbital, θ the spin of the electron. The $L_+S_- + L_-S_+$ operator in eq. (9) performs a spin-flip and this process is accompanied by a change in the orbital due to the L_+/L_- raising/lowering operator. Therefore, two orbitals of opposite spins in SOC have to be different spatial components, but

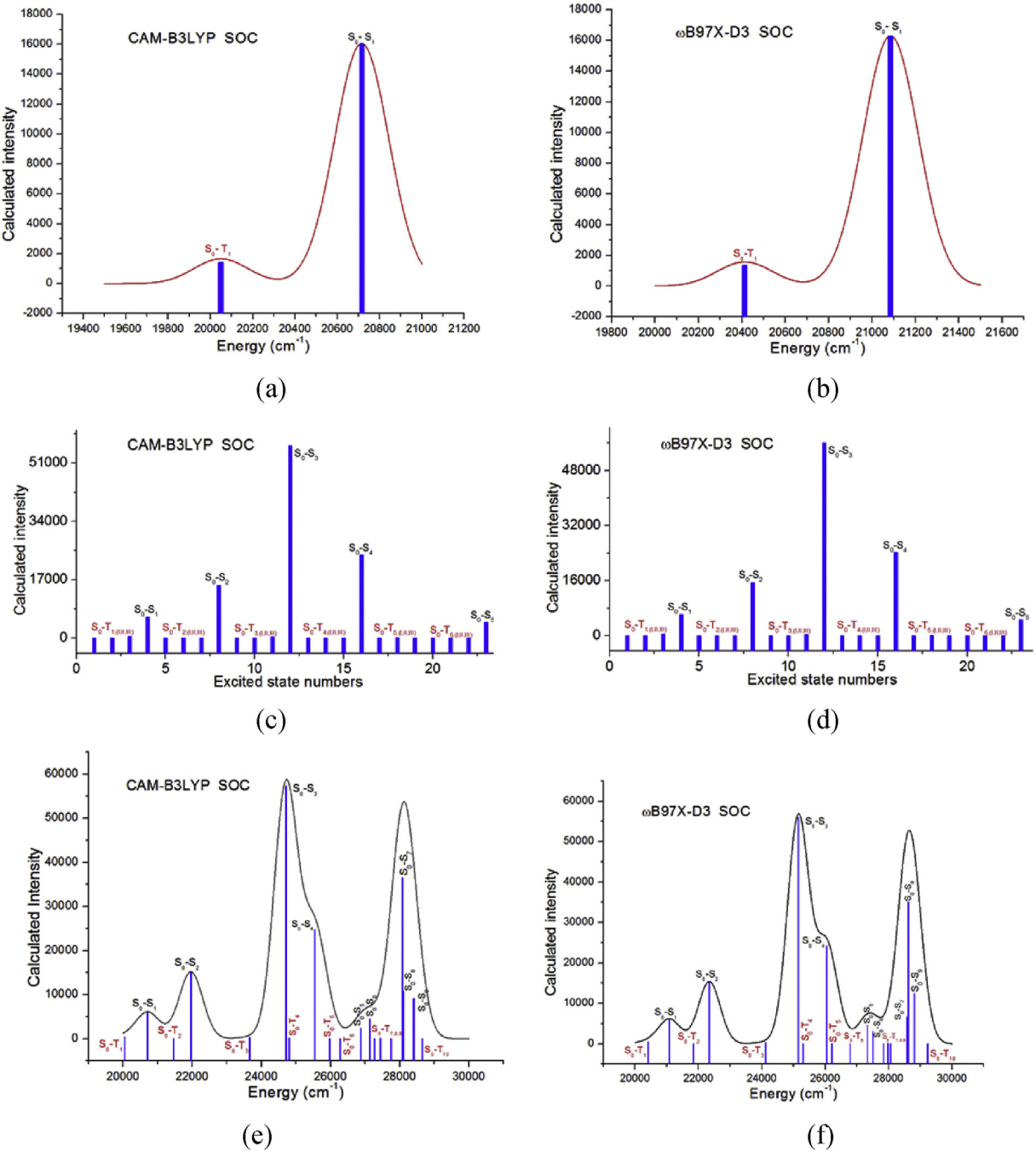

Fig. 4. Absorption spectra obtained at the scalar relativistic CAM-B3LYP(and ωB97X-D3)/ROCIS level and including SOC effects by means of QDPT. (a) and (b) are the vital spin-allowed S_0-S_1 and spin-forbidden S_0-T_1 transitions; (c) and (d) for all transitions below excited energy of S_5 state including ZFS effects; (e) and (f) considered the ten singlet and triplet excited states, respectively.

for the triplet state T_1, its wave function cannot meet this rule: i.e., two orbitals of opposite spins in the SOC interaction have the same spatial orbits. These analysis is very consistent with the values calculated ($\langle T_1|\widehat{H}_{SOC}|S_1\rangle = SOCC = 1.29\ \ cm^{-1}$ at the S_1 geometry; $\langle T_1|\widehat{H}_{SOC}|S_1\rangle = SOCC = 2.65\ \ cm^{-1}$ at the T_1 geometry, see Table 2). These analysis results show that their mutual spin-orbit interaction is rather small and vibronic effects may have to be taken into account.

Here, the vibrational contributions to ISC and RISC rates were also calculated using the TVCF method in the MOMAP program [33,34]. Upon a RISC, the geometry of the system changes via vibrational relaxations. To solve vibration correlation functions, the Huang-Rhys factors (S) and related reorganization energy (λ) must be estimated. The total intramolecular reorganization energy, λ_{intra}, can be represented as a sum of contributions from individual vibrational normal modes, i, as:

$$\lambda_{intra} = \sum \lambda_i = \sum \hbar\omega_i S_i \tag{10}$$

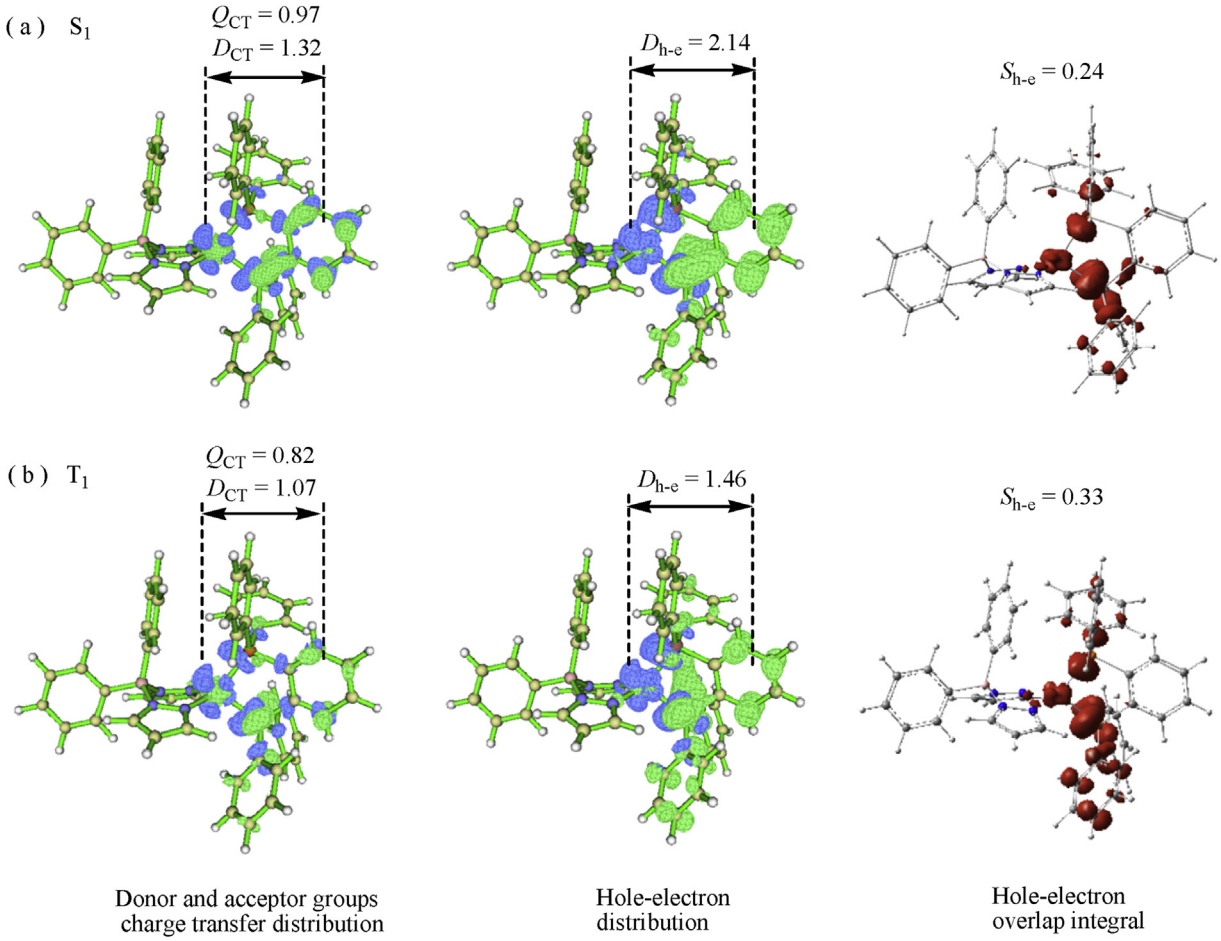

Fig. 5. Computed CT and hole-electron indexes of the mononuclear Cu(dppb)(pz_2Bph_2) system for selected S_1 and T_1 states at CAM-B3LYP/6-311+G(d, p) theoretical level. Length between donor and acceptor groups, D_{CT}, charge Q_{CT} are Å and a.u., respectively. Distance between centroid of hole and electron, $D_{h\text{-}e}$ in Å and hole-electron overlap integral $S_{h\text{-}e}$ is a.u.

$$S_i = \frac{\omega_i D_i^2}{2\hbar} \tag{11}$$

where S_i, and ω_i, denote the Huang-Rhys factor and vibrational frequency for the normal mode i, respectively; D_i is the coordinate displacement from the T_1 equilibrium position to the S_1 one along the mode i. Thus, Huang-Rhys factor is a useful measure for the extent of geometry relaxation between T_1 and S_1 states. For T_1 to S_1, the Huang-Rhys factors and reorganization energy are shown in Fig. 6 with the largest reorganization energies were embedded in the pictures, the vibronic coupling is weak, presenting very small Huang-Rhys factor, which lead to small reorganization relaxation energy of $\lambda_{intra} = 105\ cm^{-1}$ for the T_1 state ($114\ cm^{-1}$, the S_1 state).

Then, the RISC and ISC rates are calculated according to eqs. (5) and (6), RISC proceeds at a rate of $K_{RISC} = 3.98 \times 10^8\ s^{-1}$ at 300 K, which is 5–6 order of magnitude larger than the mean phosphorescence rate, $K_{P,\ av} = 0.73 \times 10^3\ s^{-1}$ (see Fig. 7). This implies that

Table 2
Calculated spin-orbit coupling matrix constants(SOCC) (cm^{-1}) between T_1 and S_n for the mononuclear Cu(dppb)(pz_2Bph_2) complex and the tensors D and E of Zero-Field splitting (ZFS) with unit in cm^{-1} in the CASSCF(8,7)/def2-TZVP(f) level.

		$\langle T_1\lvert\hat{H}_{SOC}\rvert S_n\rangle$			SOCC[a]	ZFS	
		x	y	z		D	E
At S_1 geometry	S_1	−0.50	−2.19	0.12	1.29	0.324	0.076
	S_2	23.00	155.58	−14.73	52.65		
	S_3	−437.76	201.04	−150.71	168.24		
	S_4	405.05	494.16	28.47	213.19		
	S_5	−24.94	76.03	147.19	55.84		
At T_1 geometry	S_1	1.16	4.43	−0.22	2.65	0.415	0.064
	S_2	23.14	107.63	−7.73	36.78		
	S_3	−425.44	233.20	−132.27	167.72		
	S_4	420.16	485.72	15.57	214.14		
	S_5	−25.76	66.65	153.15	56.33		

[a] $SOCC = \sqrt{(\left|\langle T_1|\hat{H}_{SOC}|S_n\rangle_x\right|^2 + \left|\langle T_1|\hat{H}_{SOC}|S_n\rangle_y\right|^2 + \left|\langle T_1|\hat{H}_{SOC}|S_n\rangle_z\right|^2)/3}$.

Table 3
Vertical energies, oscillator strength f, radiative rates, and lifetimes τ at the S_1 and T_1 minimum at the CAM-B3LYP-D3BJ/ROCIS/def2-TZVP(-f) levels.

State	ΔE (cm^{-1})	f	rate (s^{-1})	τ (μs)
At S_1 geometry				
$T_{1,\ I}$	22381.31	2.88×10^{-7}	9.62×10^1	10395
$T_{1,\ II}$	22381.32	3.91×10^{-6}	1.31×10^3	763
$T_{1,\ III}$	22381.35	6.09×10^{-6}	2.04×10^3	490
Average			$K_{P,av} = 1.15 \times 10^3$	$\tau_{av} = 870$
S_1	22735.74	1.45×10^{-2}	5.01×10^6	0.199
At T_1 geometry				
$T_{1,\ I}$	22576.13	2.43×10^{-7}	8.26×10^1	12106
$T_{1,\ II}$	22576.13	1.73×10^{-6}	5.88×10^2	1701
$T_{1,\ III}$	22576.16	5.96×10^{-6}	2.03×10^3	493
Average			$K_{P,av} = 9.01 \times 10^2$	$\tau_{av} = 1109$
S_1	22948.66	2.28×10^{-2}	8.06×10^6	0.124

the S_1 state can be populated from the T_1 state. At the same time, the ISC rate $K_{ISC} = 3.06 \times 10^9\ s^{-1}$ is again about 3 order of magnitude larger than the fluorescence rate $K_F = 6.47 \times 10^6\ s^{-1}$. Therefore, at 300 K, the S_1 and T_1 state populations rapidly equilibrate before decaying radiatively. When the temperature is set to 30 K, the situation will change. The RISC rate becomes very small, about $K_{RISC} = 1.19 \times 10^1\ s^{-1}$, while the ISC rate only decreases slightly from $K_{ISC} = 3.06 \times 10^9\ s^{-1}$ to $K_{ISC} = 1.93 \times 10^9\ s^{-1}$ (see Fig. 8). The phosphorescence rate $K_{P,\,av} = 8.09 \times 10^2\ s^{-1}$ (see Table 4), is in good agreement with the experiment value of $8.31 \times 10^2\ s^{-1}$ at low temperature. Thus, TADF should not be taken place.

In addition, we also found that K_{RISC} is several orders of magnitude smaller than $K_F = 7.12 \times 10^6\ s^{-1}$ (Fig. 8 and Table 4) and $K_{ISC} = 1.93 \times 10^9\ s^{-1}$ at 30 K, shows that their ratio reaches a level close to this kinetic limit case. Compared with room temperature, $K_{ISC} >> K_F + K^S_{nr}$ and $K_{RISC} >> K_P + K_{ISC0,}$ these limits are obviously satisfied. For the non-radiative decay, we have not computed the internal conversion rate constant, K^S_{nr} for the $S_1 \rightarrow S_0$ and ISC K_{ISC0} rate from T_1 to S_0 due to the substantial relaxation energy gap. It is know that the non-radiative decay partly including the energy dissipation through vibronic coupling can be evaluated by the normal mode reorganization energy. In order to support the above views, the calculated reorganization energies for nonradiative transition processes of T_1 to S_0 and S_1 to S_0 are shown in Fig. 9, (Corresponding shift vectors and Huang-Rhys factors are plotted Figure S2 and S3), the total reorganization energy (λ_{intra}) at the ground and excited states can be obtained through eq. (10). From Fig. 9, the vibration normal modes with large λ_{intra} occur high frequency regions, 500 cm^{-1} to 1700 cm^{-1}. We found that the large contributions to the total λ_{intra} from the twisting vibration of between the P5—Cu—P6 plane and N1—Cu—N2 plane and from Cu—P bond stretching vibration. The λ_{intra} values of the T_1 state is 283827 cm^{-1}(or 35.19 eV), and for the S_1 state is 78223 cm^{-1} (or 9.69 eV). The deviations of between S_0 and S_1 or T_1 geometries are mainly attributed to the twist of between the P5—Cu—P6 plane and N1—Cu—N2 plane and the Cu—P bond lengthen, which will lead to these processes of T_1 to S_0 and S_1 to S_0 is to be much slower than the radiative decay rates and will be neglected. Therefore, the equilibrium limit, $K_{ISC} >> K_F + K^S_{nr}$ and $K_{RISC} >> K_P + K_{ISC0,}$ can be rewritten as $K_{ISC} >> K_F$ and $K_{RISC} >> K_{P,}$ here, $K_{ISC} >> K_F$ is certainly adequate at all temperature regions, but the second limit, $K_{RISC} >> K_P$ is not.

For deeper understanding of the emission properties and the equilibrium conditions, decay time as a function of temperature in the range from 10 K to 300 K is calculated using the formula fitted by many experimentalists of eq. (12) [2], the calculated results are plotted in Fig. 10.

$$\tau(T) = \frac{3 + \exp[-\Delta E(S_1 - T_1)/k_B T]}{\frac{3}{\tau(T_1)} + \frac{1}{\tau(S_1)}\exp[-\Delta E(S_1 - T_1)/k_B T]} \tag{12}$$

In this equation, k_B represents the Boltzmann constant, and $\tau(T_1)$

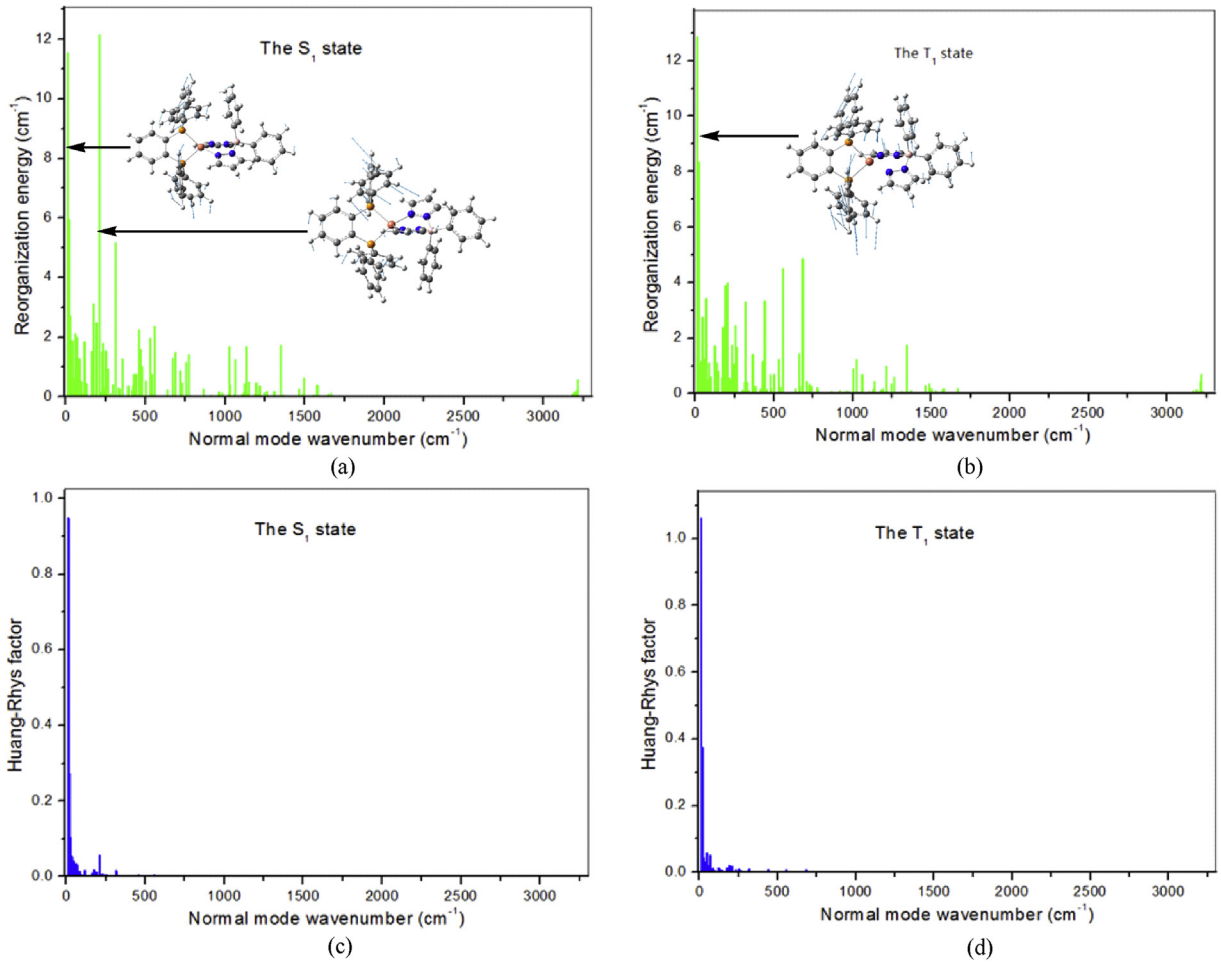

Fig. 6. Calculated Huang-Rhys factors and reorganization energies versus the normal modes in term of the corresponding S_1 and T_1 potential surfaces and the normal modes with the largest reorganization energies were embedded in the pictures.

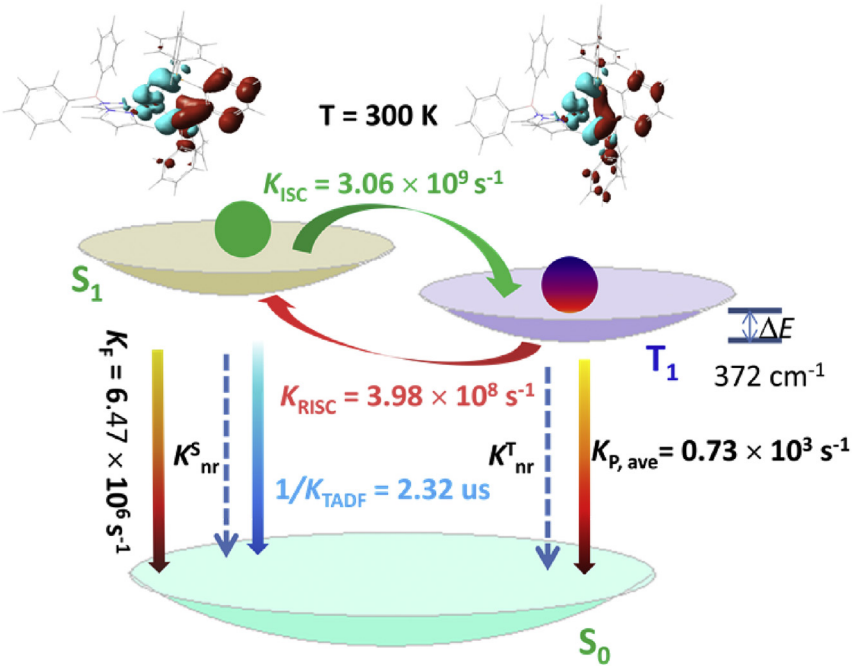

Fig. 7. Fluorescence (K_F), phosphorescence (K_P), and ISC (K_{ISC}) rates at 300 K for the global T_1 minimum. Electronic density change induced by excitations of the S_0 to S_1 and T_1 states was inserted in the top (In light blue, loss; In deep rose, gain). (For interpretation of the references to colour in this figure legend, the reader is referred to the web version of this article.)

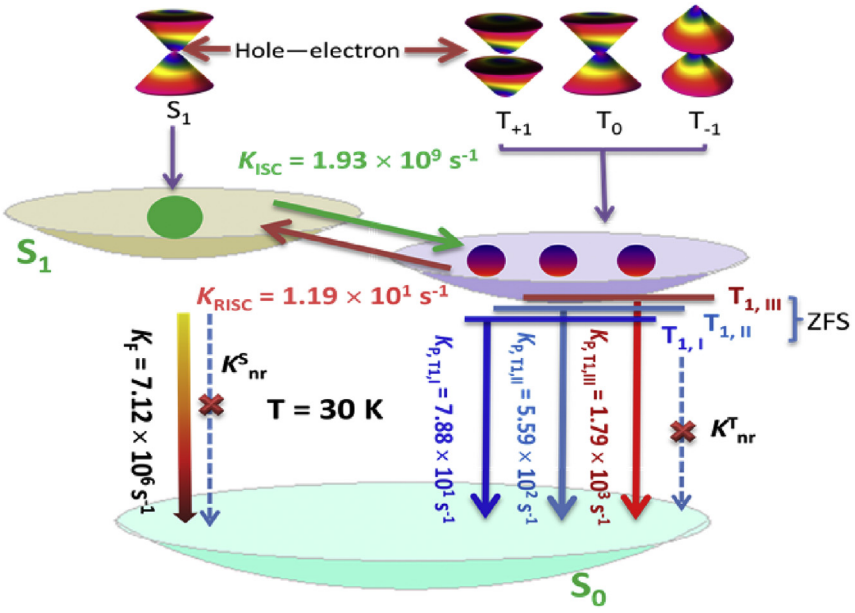

Fig. 8. Exciton dynamic processes for a typical TADF emitter in OLEDs. Singlet and triplet excitons are generated in a 1: 3 ratio depending on the spin degeneracy. K_F, K_P, K_{ISC}, and K_{RISC} are rate constants of fluorescence, phosphorescence, intersystem crossing, and reverse intersystem crossing at 30 K for the global T_1 minimum.

Table 4
At different temperature, calculated vertical energies, radiative rates, and lifetimes τ at the T_1 minimum at the CAM-B3LYP-D3BJ levels including thermal vibration activation.

State	ΔE (cm^{-1})	30 K		80 K		300 K	
		rate (s^{-1})	τ (μs)	rate (s^{-1})	τ (μs)	rate (s^{-1})	τ (μs)
$T_{1, I}$	22576.13	7.88×10^1	12694	7.73×10^1	12934	7.07×10^1	14143
$T_{1, II}$	22576.13	5.59×10^2	1789	5.48×10^2	1823	5.02×10^2	1993
$T_{1, III}$	22576.16	1.79×10^3	558	1.76×10^3	568	1.61×10^3	621
Average		8.09×10^2	1236	7.95×10^2	1258	7.27×10^2	1375
S_1	22948.66	7.12×10^6	0.139	7.07×10^6	0.141	6.47×10^6	0.155

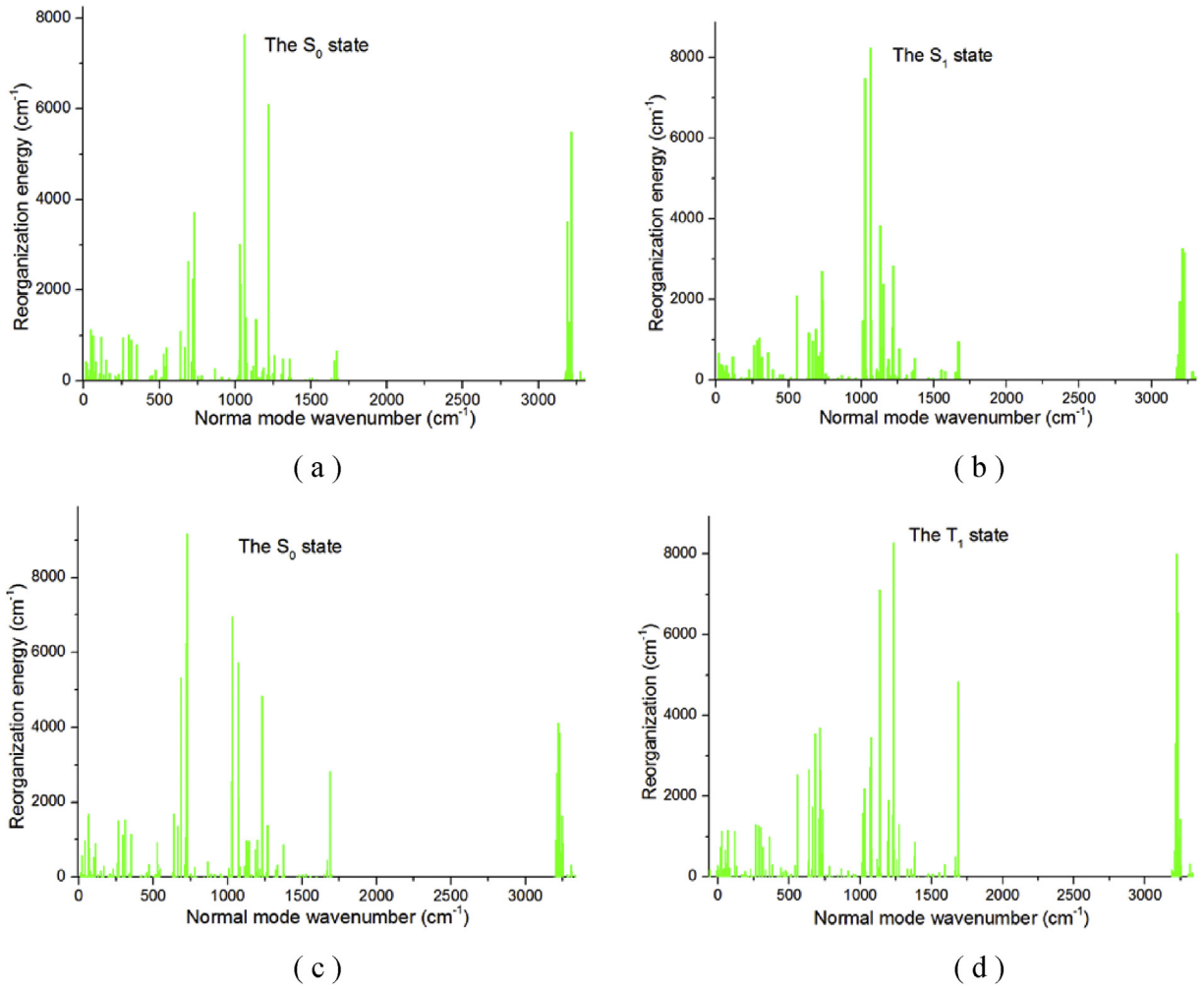

Fig. 9. Calculated reorganization energies versus the normal modes in term of the corresponding potential surface. The S_0 and S_1 states are plotted in (a) and (b); (c) and (d) for the S_0 and T_1 states.

and $\tau(S_1)$ are the emission decay times of the T_1 and S_1, respectively, in the absence of thermalization. At very low temperature, the exponential terms disappear and the decay time $\tau(T)$ equals the phosphorescence decay time $\tau(T_1)$, while at high temperature, the term containing $\tau(T_1)$ can be neglected and one essential obtains the decay time of TADF fluorescence.

For the mononuclear Cu(dppb)(pz_2Bph_2) system, the emission decay time is almost constant and one observes a plateau with $\tau(T_1) \approx 1111.05$ μs in the temperature range from 10 K to 50 K. This emission is assigned as phosphorescence from the T_1 to S_0. With temperature increase, a large reduction of decay time is estimated since a thermal activation of a higher-lying state leads to be significantly more allowance of the transition to the S_0 state than the T_1 state. At $T > 150$ K, the contribution of the S_1 state to the emission dominates, this effect represents a TADF. Computed decay time is $\tau(300\ K) = 2.32$ μs by fitting equation (12), the experimental value of 3.3 μs [22].

4. Conclusions

In this study, the geometries and photophysical properties of a mononuclear Cu(dppb)(pz_2Bph_2) complex were computationally investigated using the quantum chemistry calculations. Absorption spectrum obtained at the scalar relativistic CAM-B3LYP/ROCIS level and including SOC effects by means of QDPT is in excellent agreement with the experimental data. Therefore, all electronic excitation energies and properties reported in this work refer to CAM-

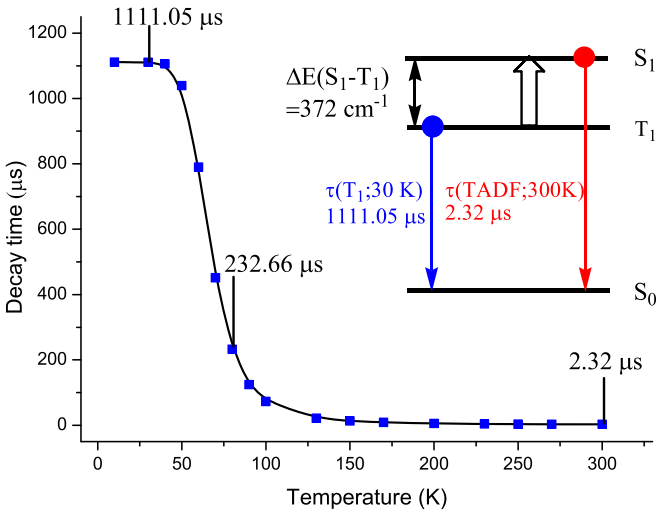

Fig. 10. Emission decay time of the mononuclear Cu(dppb)(pz_2Bph_2) complex versus temperature from 10 K to 300 K.

B3LYP/ROCIS values.

The lowest excited singlet S_1 and triplet T_1 states are designated as ^{1,3}MLCT from $d/\sigma \rightarrow \pi^*$ MLCT excitations. It was found that the S_1 and T_1 possess separated hole-electron with small electron overlap $S_{h\text{-}e}$ and long distance $D_{h\text{-}e}$, leading to small $\Delta E(S_1\text{-}T_1)$. Indeed, the experimentally determined values amount only to 370 cm^{-1}, which is in good agreement with calculated value of 371 cm^{-1} for the CAM-B3LYP method. As a consequence, the Cu(dppb)(pz_2Bph_2) complex is highly attractive candidates for studies and applications of TADF.

In order to ascertainably TADF take place, the S_1 state has to be repopulated. That means that the RISC rate has to be larger than the rates of radiative and nonradiative decay of the T_1 state to the S_0 state. However, the S_1 and T_1 states arise from the same orbital excitation, their mutual spin-orbit interaction is forbidden and vibronic effects have to be considered. In this work, the photophysical properties including the radiative and the nonradiative decay rates arising from SOC of the excited states have been investigated theoretically using the TVCF method. The calculated results show that RISC proceeds at a rate of $K_{RISC} = 3.98 \times 10^8\ s^{-1}$ at 300 K, which is about 6 order of magnitude larger than the mean phosphorescence rate, $K_{P,\,av} = 7.3 \times 10^2\ s^{-1}$. This implies that the S_1 state can be populated from the T_1 state. At the same time, the ISC rate $K_{ISC} = 3.06 \times 10^9\ s^{-1}$ is again about 3 order of magnitude larger than the fluorescence rate $K_F = 6.47 \times 10^6\ s^{-1}$. Therefore, at 300 K, the S_1 and T_1 state populations rapidly equilibrate before decaying radiatively. Computed TADF decay time is $\tau(300\ K) = 2.32\ \mu s$ by fitting using equation (12), the experimental value of 3.3 μs. When the temperature is set to 30 K, the situation will change. The RISC rate becomes very small, about $K_{RISC} = 1.19 \times 10^1\ s^{-1}$, while the ISC rate only decreases slightly from $K_{ISC} = 3.06 \times 10^9\ s^{-1}$ to $K_{ISC} = 1.93 \times 10^9\ s^{-1}$. The phosphorescence rate $K_{P,\,av} = 8.09 \times 10^2\ s^{-1}$, is in good agreement with the experiment value of $8.31 \times 10^2\ s^{-1}$ at low temperature. Thus, TADF should not be taken place.

Acknowledgements

The authors gratefully acknowledge financial support from National Natural Science Foundation of China (Grant No. 21263022, 21663025, 21663024).

Appendix A. Supplementary data

Supplementary data related to this article can be found at http://dx.doi.org/10.1016/j.orgel.2017.09.017.

References

[1] Y. Tao, K. Yuan, T. Chen, P. Xu, H.H. Li, R.F. Chen, C. Zheng, L. Zhang, W. Huang, Thermally activated delayed fluorescence materials towards the breakthrough of organoelectronics, Adv. Mater. 47 (2014) 7931–7956.
[2] H. Yersin, A.F. Rausch, R. Czerwieniec, T. Hofbeck, T. Fischer, The triplet state of organo-transition metal compounds. Triplet harvesting and singlet harvesting for efficient OLEDs, Coord. Chem. Rev. 255 (2011) 2622–2652.
[3] T. Ogiwara, Y. Wakikawa, T. Ikoma, Mechanism of intersystem crossing of thermally activated delayed fluorescence molecules, J. Phys. Chem. A 119 (2015) 3415–3418.
[4] S. Perumal, B. Minaev, H. Ågren, Triplet state phosphorescence in Tris(8-hydroxyquinoline) Aluminum light emitting diode materials, J. Phys. Chem. C 117 (2013) 3446–3455.
[5] M.A. Baldo, D. O'brien, Y. You, A. Shoustikov, S. Sibley, M. Thompson, S. Forrest, Highly efficient phosphorescent emission from organic electroluminescent devices, Nature 395 (1998) 151–154.
[6] C. Adachi, M.A. Baldo, M.E. Thompson, S.R. Forrest, Nearly 100% internal phosphorescence efficiency in an organic light-emitting device, J. Appl. Phys. 90 (2001) 5048–5505.
[7] B. Zhao, T. Zhang, B. Chu, W. Li, Z. Su, Y. Luo, R. Li, X. Yan, F. Jin, Y. Gao, Highly efficient tandem full exciplex orange and warm white OLEDs based on thermally activated delayed fluorescence mechanism, Org. Electron. 17 (2015) 15–21.
[8] H. Uoyama, K. Goushi, K. Shizu, H. Nomura, C. Adachi, Highly efficient organic light-emitting diodes from delayed fluorescence, Nature 492 (2012) 234–238.
[9] T. Chen, L. Zheng, J. Yuan, Z.F. An, R.F. Chen, Y. Tao, H.H. Li, X.J. Xie, W. Huang, Understanding of the control of singlet-triplet splitting for organic exciton manipulating: a combined theoretical and experimental approach, Sci. Rep. 5 (2015) 10923.
[10] R. Czerwieniec, M.J. Leitl, H.H.H. Homeier, H. Yersin, Cu(I) complexes-Thermally activated delayed fluorescence. Photophysical approach and material design, Coord. Chem. Rev. 325 (2016) 2–28.
[11] J.C. Deaton, S.C. Switalski, D.Y. Kondakov, R.H. Young, T.D. Pawlik, D.J. Giesen, S.B. Harkins, A.J.M. Miller, S.F. Mickenberg, J.C. Peters, E-Type delayed fluorescence of a phosphine-supported $Cu_2(\mu\text{-}NAr_2)_2$ diamond core: harvesting singlet and triplet excitons in OLEDs, J. Am. Chem. Soc. 132 (2010) 9499–9508.
[12] M.J. Leitl, V.A. Krylova, P.I. Djurovich, M.E. Thompson, H. Yersin, Phosphorescence versus thermally activated delayed fluorescence. Controlling singlet–triplet splitting in brightly emitting and sublimable Cu(I) compounds, J. Am. Chem. Soc. 136 (2014) 16032–16038.
[13] F. Dumur, Recent advances in organic light-emitting devices comprising copper complexes: a realistic approach for low-cost and highly emissive devices? Organ. Electron. 21 (2015) 27–39.
[14] T. Hofbeck, U. Monkowius, H. Yersin, Highly Efficient luminescence of Cu(I) compounds: thermally activated delayed fluorescence combined with short-lived phosphorescence, J. Am. Chem. Soc. 137 (2015) 399–404.
[15] A.N. Gusev, V.F. Shul'gin, B.F. Minaev, G.V. Baryshnikov, V.A. Minaevab, A.T. Baryshnikova, M.A. Kiskin, I.L. Eremenko, Synthesis and luminescent properties of copper(I) complexes with 3-pyridin-2-yl-5-(4-R-phenyl)-1*H*-1,2,4-triazoles, Russ. J. Inorg. Chem. 62 (2017) 423–430.
[16] V.A. Minaeva, B.F. Minaev, G.V. Baryshnikov, Calculation of the optical spectra of the copper(I) complex with triphenylphosphine, iodine, and 3-pyridine-2-yl-5-phenyl-1*H*- 1,2,4-triazole by the DFT method, Opt. Spectrosc. 122 (2017) 175–183.
[17] F.B. Dias, K.B. Bourdakos, V. Jankus, K.C. Moss, K.T. Kamtekar, V. Bhalla, J. Santos, M.R. Bryce, A.P. Monkman, Triplet harvesting with 100% efficiency by way of thermally activated delayed fluorescence in charge transfer OLED Emitters, Adv. Mater. 25 (2013) 3707–3714.
[18] T. Ogiwara, Y. Wakikawa, T. Ikoma, Mechanism of intersystem crossing of thermally activated delayed Fluorescence Molecules, J. Phys. Chem. A 119 (2015) 3415–3418.
[19] M.K. Etherington, J. Gibson, H.F. Higginbotham, T.J. Penfold, A.P. Monkman, Revealing the spin-vibronic coupling mechanism of thermally activated delayed fluorescence, Nat. Commun. 7 (2016) 13680.
[20] J. Gibson, A.P. Monkman, T.J. Penfold, The importance of vibronic coupling for efficient reverse intersystem crossing in thermally activated delayed fluorescence molecules, ChemPhysChem 17 (2016) 2956–2961.
[21] J. Foller, M. Kleinschmidt, C.M. Marian, Phosphorescence or thermally activated delayed fluorescence? Intersystem crossing and radiative rate constants of a three-coordinate copper(I) complex determined by quantum-chemical methods, Inorg. Chem. 55 (2016) 7506–7516.
[22] R. Czerwieniec, H. Yersin, Diversity of copper(I) complexes showing thermally activated delayed fluorescence: basic photophysical analysis, Inorg. Chem. 54 (2015) 4322–4327.
[23] S. Igawa, M. Hashimoto, I. Kawata, M. Yashima, M. Hoshinoa, M. Osawa, Highly efficient green organic light-emitting diodes containing luminescent tetrahedral copper(I) complexes, J. Mater. Chem. C 1 (2013) 542–551.
[24] Q. Peng, Y.L. Niu, Q. Shi, X. Gao, Z.G. Shuai, Correlation function formalism for triplet excited state decay: combined spin-orbit and nonadiabatic couplings, J. Chem. Theory Comput. 9 (2013) 1132–1143.
[25] T. Yanai, D. Tew, N. Handy, A new hybrid exchange-correlation functional using the Coulomb-attenuating method (CAM-B3LYP), Chem. Phys. Lett. 393 (2004) 51–57.
[26] J.D. Chai, M. Head-Gordon, Systematic optimization of long-range corrected hybrid density functionals, J. Chem. Phys. 128 (2008) 084106.
[27] S. Grimme, J. Antony, S. Ehrlich, H. Krieg, A consistent and accurate *ab initio* parametrization of density functional dispersion correction (DFT-D) for the 94 elements H-Pu, J. Chem. Phys. 132 (2010) 154104.
[28] M.J. Frisch, G.W. Trucks, H.B. Schlegel, et al., Gaussian 09, Revision-D.01, Gaussian Inc, Wallingford, CT, 2009.
[29] M. Roemelt, F. Neese, Excited states of large open-shell molecules: an efficient, general, and spin-adapted approach based on a restricted open-shell ground state wave function, J. Phys. Chem. A 117 (2013) 3069–3083.
[30] F. Neese, The ORCA program system, WIREs Comput. Mol. Sci. 2 (2012) 73–78.
[31] F. Neese, F. Wennmohs, A. Hansen, U. Becker, Efficient approximate and parallel Hartree–Fock and hybrid DFT calculations. A 'chain-of-spheres' algorithm for the Hartree–Fock exchange, Chem. Phys. 356 (2009) 98–109.
[32] B. Sandhoefer, F. Neese, One-electron contributions to the g-tensor for second-order Douglas-Kroll-Hess theory, J. Chem. Phys. 137 (2012) 094102.
[33] F. Neese, Efficient and accurate approximations to the molecular spin-orbit coupling operator and their use in molecular g-tensor calculations, J. Chem. Phys. 122 (2005), 034107/034101–034113.
[34] B. Minaev, G. Baryshnikov, H. Agren, Principles of phosphorescent organic light emitting devices, Phys. Chem. Chem. Phys. 16 (2016) 1719–1758.
[35] G. Baryshnikov, B. Minaev, H. Ågren, Theory and calculation of the phosphorescence phenomenon, Chem. Rev. 117 (2017) 6500–6537.

[36] Q. Peng, Y.P. Yi, Z.G. Shuai, J.S. Shao, Excited state radiationless decay process with Duschinsky rotation effect: formalism and implementation, J. Chem. Phys. 126 (2007) 114302.
[37] Y.L. Niu, Q. Peng, C.M. Deng, X. Gao, Z.G. Shuai, Theory of excited state decays and optical spectra: application to polyatomic molecules, J. Phys. Chem. A 114 (2010) 7817–7831.
[38] T. Lu, F. Chen, Multiwfn: a multifunctional wavefunction analyzer, J. Comput. Chem. 33 (2012) 580–592.
[39] D. Danovich, S. Shaik, Spin–orbit coupling in the oxidative activation of H–H by FeO+. selection rules and reactivity effects, J. Am. Chem. Soc. 119 (1997) 1773–1786.